

FACULTY
OF MATHEMATICS
AND PHYSICS
Charles University

BACHELOR THESIS

Klára Anna Šindlerová

Modeling the regional depressions on the surface of Saturn's moon Enceladus

Department of Geophysics

Supervisor of the bachelor thesis: prof. RNDr. Ondřej Čadek, CSc.

Study programme: Mathematical Modelling

Prague 2025

I declare that I carried out this bachelor thesis on my own, and only with the cited sources, literature and other professional sources. I understand that my work relates to the rights and obligations under the Act No. 121/2000 Sb., the Copyright Act, as amended, in particular the fact that the Charles University has the right to conclude a license agreement on the use of this work as a school work pursuant to Section 60 subsection 1 of the Copyright Act.

In ..... date ....

Author's signature

To everyone whose patience made this thesis possible.

In particular, I would like to thank the supervisor of this thesis, prof. RNDr. Ondřej Čadek, CSc., for introducing me to the fascinating world of icy moons and for all the knowledge he shared. An equally important role was played by my advisor, Mgr. Martin Kihoulou, DiS., who spent countless hours helping me overcome the challenges of Python, FEniCS, and even taught me how to use Midnight Commander. I am also grateful to doc. RNDr. Ondřej Souček, Ph.D., for carefully reading through the methodological part and providing valuable suggestions.

Last but not least, I thank my family and Rosťa for patiently listening to my rambling about Enceladus—usually enthusiastic, though occasionally frustrated.

Title: Modeling the regional depressions on the surface of Saturn's moon Enceladus

Author: Klára Anna Šindlerová

Department: Department of Geophysics

Supervisor: prof. RNDr. Ondřej Čadek, CSc., Department of Geophysics

Abstract: This thesis investigates the formation of large depressions on the surface of Enceladus, Saturn's icy satellite, through numerical modeling of thermal convection and phase changes at the ice-ocean interface. Using custom code developed in Python with the FEniCS software package, various scenarios were simulated to understand the mechanisms driving these 100-km-scale depressions. The results indicate that a strong heat flux from the ocean, generated by tidal dissipation within Enceladus' porous silicate core, is the most probable cause. The model predicts depression develop over approximately 10 million years. The results show that this mechanism may also be responsible for the creation of brittle fractures on Enceladus' South Pole, called Tiger Stripes. The conclusions presented in the thesis are based on 2D simulations in a Cartesian box and the use of a simplified, temperature-dependent rheology, and need to be verified by more realistic simulations in spherical geometry.

Keywords: deformation of ice, phase transitions, Enceladus

Název práce: Modelování regionálních depresí na povrchu Saturnova ledového měsíce Enceladu

Autor: Klára Anna Šindlerová

Katedra: Katedra geofyziky

Vedoucí bakalářské práce: prof. RNDr. Ondřej Čadek, CSc., Katedra geofyziky

Abstrakt: Tato práce se zabývá zkoumáním vzniku rozsáhlých depresí na povrchu Enceladu, ledového měsíce planety Saturn, prostřednictvím numerického modelování rovnic termální konvekce a fázových přechodů. Pomocí vlastního kódu vytvořeného v Pythonu, s využitím softwarového balíku FEniCS, bylo simulováno několik scénářů s cílem porozumět mechanismům zodpovědným za vznik těchto depresí o rozměrech kolem 100 km. Výsledky naznačují, že příčinou je silný tepelný tok z oceánu, generovaný slapovou disipací v jádře. Model predikuje, že tyto útvary vznikají na časové škále okolo 10 milionů let. Výsledky také ukazují, že tento mechanisms může být zodpovědný i za vznik zlomových struktur na jižním pólu, zvaných Tygří pásy. Model nicméně obsahuje určitá omezení, včetně zjednodušené 2D geometrie a reologie ledu závislé pouze na teplotě. Závěry práce je proto potřeba verifikovat za pomoci realističtějších simulací ve sférické geometrii.

Klíčová slova: deformace ledu, fázové přechody, Enceladus

Contents

Introduction **6**

1 Method **8**
1.1 Governing equations 8
1.2 Computational domain and boundary conditions 9
1.3 Weak form 11
1.4 Model setup in FEniCS 13
1.5 Program testing 16

2 Results **21**
2.1 Parametric study 21
2.2 Typical simulation 23
2.3 Effect of the ice shell thickness 24
2.4 Effect of heat flux anomaly width 24
2.5 Results for the end-member thickness 26
2.6 Will the ice shell break? 26

Discussion and Conclusions **28**

Bibliography **29**

List of Figures **31**

List of Tables **32**

Introduction

Enceladus, one of Saturn's satellites, falls into the category of icy moons (see Figure 1). These planetary bodies are studied for a simple reason: humanity has always sought life outside our small planet, and icy moons may be the closest objects with habitable conditions. Modeling the surface of these bodies provides insights into the conditions in the liquid water ocean beneath the ice shell.

Although small, with a radius of only 252 km, Enceladus has been intensely studied. Observations from the Cassini mission (2004–2017) detected that the moon is generating a surprisingly large amount of thermal power [16–50 GW, Souček et al., 2019]. Due to its structure, with an average density of 1610 $\mathrm{kg\,m^{-3}}$ and a 70-km-thick hydrosphere overlying a porous silicate core, the only possible source of this heat is tidal dissipation [Choblet et al., 2017]. Measuring the physical libration of Enceladus [Thomas et al., 2016] and analysis of particles ejected by Enceladus' geysers discovered by Cassini [Postberg et al., 2009] indicate that the thickness of the subsurface ocean is approximately 45 kilometers. The thickness of the ice shell above ranges from 5 to 35 km, with these variations likely caused by large changes in the heat flux from the ocean [Čadek et al., 2016].

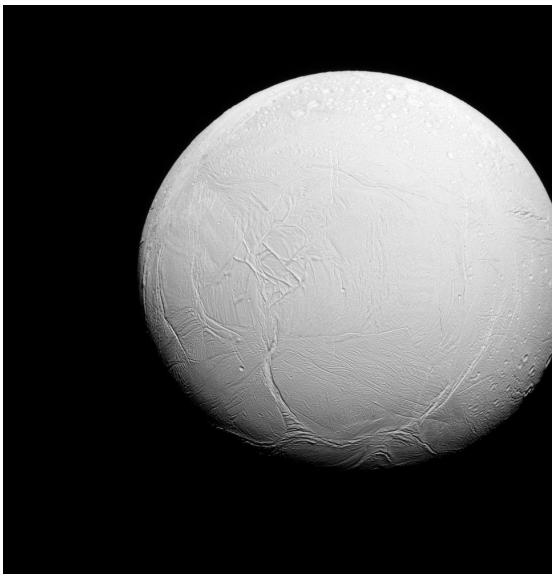


Figure 1 A Tale of Two Hemispheres [NASA/JPL-Caltech/Space Science Institute, 2015].

The main research focus on Enceladus was always the South Pole Region and its geysers gushing out from a series of fractures called Tiger Stripes. However, a recent analysis of topographic data from the Cassini mission has revealed depressions with a diameter larger than 100 km and a depth of nearly 3.5 km [Park et al., 2024] (see Figure 2). The depressions are too smooth to be created by impact or tectonically [Park et al., 2024, Schenk and McKinnon, 2024]. The absence of a clear cause of the depressions naturally raised questions, therefore the origin of these 100-km-scale depressions is yet to be explained. According to Schenk and McKinnon [2024], the most likely reason behind this is an isostatic response of the floating ice shell to the thickness variations, which might be caused by hydrothermal heat generated by tidal dissipation in the core.

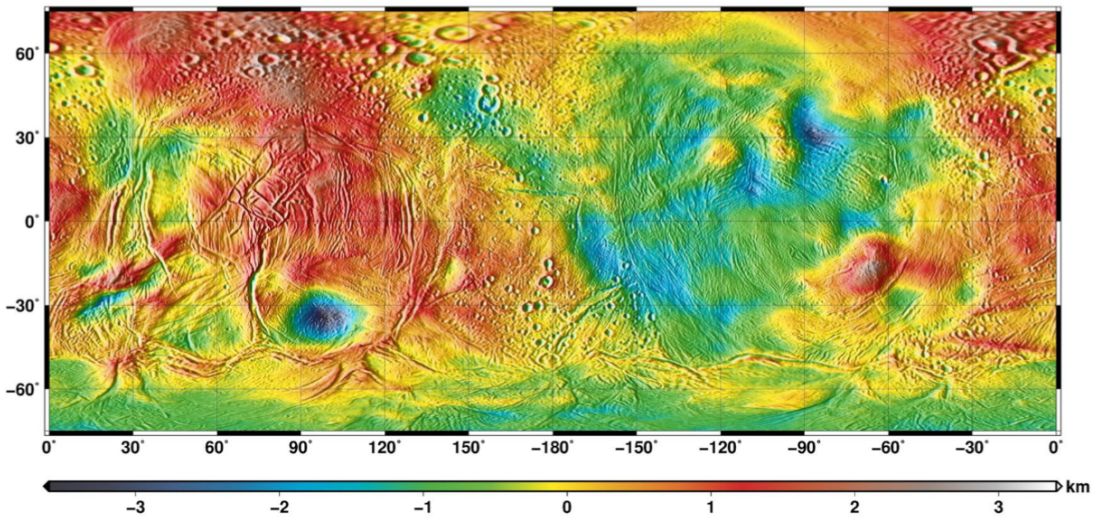


Figure 2 Topography of Enceladus [Park et al., 2024].

In this thesis, I will investigate the mechanisms behind the formation of these depressions. Based on the previous research and physical analysis, I will formulate one of the possible scenarios and model it using finite element method (FEM). The objective of this thesis is to present and discuss physical mechanisms that may be responsible for these depressions.

1 Method

1.1 Governing equations

In this study, I investigate the deformation of an ice layer caused by variations in the heat flux from the ocean underneath. The task is described by the equations of thermal convection in the Boussinesq approximation [e.g., Kihoulou et al., 2023]:

$$\nabla \cdot \vec{v} = 0\,, \tag{1.1}$$

$$\nabla \cdot \boldsymbol{t} + \rho_0 \vec{g}[1 - \alpha(T - T_m)] = \vec{0}\,, \tag{1.2}$$

$$\rho_0 c_p \frac{\partial T}{\partial t} = \nabla \cdot (k \nabla T) - \rho_0 c_p (\vec{v} \cdot \nabla T) + Q\,, \tag{1.3}$$

$$\boldsymbol{t} = -p\boldsymbol{I} + \eta(\nabla \vec{v} + (\nabla \vec{v})^T)\,, \tag{1.4}$$

where the meaning of the symbols is explained in Table 1.1. I do not include the inertial force in the momentum equation (see Equation 1.2) because the Prandtl number of ice is very large ($> 10^5$) therefore the impact of the inertial force on the ice flow is negligible.

It is commonly assumed that on a geological time scales, the ice behaves as a viscous fluid. The viscosity of ice generally depends on temperature, stress, and grain size [Goldsby and Kohlstedt, 2001]. For simplicity, I will neglect the influence of stress and grain size, and assume that the viscosity depends only on temperature [cf. Souček et al., 2019],

$$\eta(T) = \eta_0 \exp\left(\frac{E}{RT_m}\left(\frac{T_m}{T} - 1\right)\right)\,. \tag{1.5}$$

At low temperatures typical for the surfaces of icy moons (around 100 K), the viscosity given by Equation 1.5 can reach very high values ($> 10^{30}$ Pa s), which can complicate the numerical solution. Therefore, η will be restricted from above by the cut-off viscosity η_{max}. Thermal conductivity k in Equation 1.3 is considered in the form [Carnahan et al., 2021]:

$$k(T) = \frac{k_1}{T}\,. \tag{1.6}$$

The specific heat c_p in Equation 1.3 is considered in the form [McCord and Sotin, 2005]:

$$c_p(T) = c_1 + c_2\,T\,. \tag{1.7}$$

The temperature dependence of the coefficient of thermal expansion α in Equation 1.2 is weak [McCord and Sotin, 2005] and I will approximate this parameter by constant. The values of all parameters are provided in Table 1.1.

Symbol	Physical property	Value	Unit
$\vec{v}$	Velocity	-	$\mathrm{m\,s^{-1}}$
$\boldsymbol{t}$	Cauchy stress tensor	-	Pa
p	Pressure	-	Pa
T	Temperature	-	K
t	Time	-	s
Q	Internal heating	-	$\mathrm{W\ m^{-3}}$
η	Viscosity	Eq. 1.5	$\mathrm{Pa\,s}$
k	Thermal conductivity	Eq. 1.6	$\mathrm{W\,m^{-1}\,K^{-1}}$
c_p	Specific heat	Eq. 1.7	$\mathrm{kJ\,kg^{-1}\,K^{-1}}$
ρ_0	Density of ice at temperature T_m	920	$\mathrm{kg\,m^{-3}}$
T_m	Melting temperature of ice	265	K
$\vec{g}$	Gravitational acceleration	0.113	$\mathrm{m\,s^{-2}}$
α	Coefficient of thermal expansion	1.6×10^{-4}	$\mathrm{K^{-1}}$
η_0	Viscosity at the melting temperature	10^{16}	$\mathrm{Pa\,s}$
E	Activation energy of diffusion creep	50	$\mathrm{kJ\,mol^{-1}}$
R	Gas constant	8.314	$\mathrm{J\,mol^{-1}\,K^{-1}}$
k_1	Constant factor in Equation 1.6	621	$\mathrm{W\,m^{-1}}$
c_1	Constant factor in Equation 1.7	185	$\mathrm{kJ\,kg^{-1}\,K^{-1}}$
c_2	Constant factor in Equation 1.7	7.037	$\mathrm{kJ\,kg^{-1}\,K^{-2}}$

Table 1.1 List of symbols and values for Chapter 1.1.

1.2 Computational domain and boundary conditions

The computational domain is initially a rectangle with an aspect ratio of 8. Such a large ratio is justified by the relatively small thickness of ice on Enceladus [5 - 35 km, Čadek et al., 2016], and the fact that the regional depression under study has a diameter of approximately 100 km. As shown in Figure 1.1, the model uses 2D Cartesian coordinates, neglecting the curvature of Enceladus' surface. This simplification is adopted to simplify formulation of the problem. While this approach may not provide fully realistic results, it serves as an initial step in determining which of the considered scenarios merit further investigation.

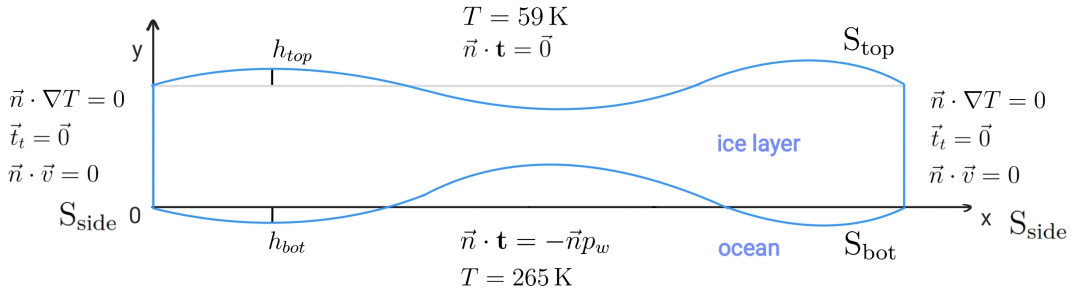


Figure 1.1 Sketch of the computational domain with boundary conditions.

As illustrated in Figure 1.1, the boundary conditions considered in this model include a free surface at the top, hydrostatic pressure at the bottom of the ice shell, and free-slip impermeable boundaries on the lateral boundaries. On the lateral boundaries, the tangential component of the traction and the normal component of the velocity are set to zero, and these boundaries are also impermeable to the heat transfer:

$$\vec{t}_t = \vec{n} \cdot \boldsymbol{t} - ((\vec{n} \cdot \boldsymbol{t}) \cdot \vec{n})\vec{n} = \vec{0}\,, \tag{1.8}$$

$$\vec{n} \cdot \vec{v} = 0\,, \tag{1.9}$$

$$\vec{n} \cdot \nabla T = 0\,. \tag{1.10}$$

At the top boundary, the ice shell interacts only with the surrounding vacuum, resulting in the absence of traction forces. Therefore, the boundary condition is expressed as:

$$\vec{t}_{(\vec{n})} = \vec{n} \cdot \boldsymbol{t} = \vec{0}\,. \tag{1.11}$$

where $\vec{n}$ is the outward-pointing unit normal vector to the surface.
The evolution of the top boundary is described by the equation of material surface:

$$\frac{\partial h_{top}}{\partial t} = v_y - \frac{\partial h_{top}}{\partial x} v_x\,, \tag{1.12}$$

where $h_{top}(x,t)$ is the topography of the surface. The temperature at the surface is

$$T = 59\,\mathrm{K}\,. \tag{1.13}$$

At the bottom boundary, the effect of hydrostatic pressure in the ocean needs to be considered in the free surface condition:

$$\vec{t}_{(\vec{n})} = \vec{n} \cdot \boldsymbol{t} = -\vec{n} p_w\,. \tag{1.14}$$

This boundary is also influenced by phase changes between ice and water, which affects the form of Equation 1.12 [Kihoulou et al., 2023]:

$$\frac{\partial h_{bot}}{\partial t} = (v_y + u_y) - \frac{\partial h_{bot}}{\partial x}(v_x + u_x)\,, \tag{1.15}$$

where

$$\vec{u} = \frac{\vec{n} \cdot (\vec{q_i} - \vec{q_w})}{\rho_0 L}\vec{n} \tag{1.16}$$

is the rate of the phase change. The temperature at the bottom boundary is set to the melting temperature of ice:

$$T = 265\,\mathrm{K}\,. \tag{1.17}$$

The meaning of the symbols in Chapter 1.2 is explained in Table 1.2.

Symbol	Meaning	Value	Unit
$\vec{t}_t$	Tangential component of traction	-	Pa
$\vec{n}$	Normal vector	-	-
$\vec{t}_{(\vec{n})}$	Traction	-	Pa
p_w	Hydrostatic pressure in the ocean	-	Pa
h_{top}, h_{bot}	Topography	-	m
$\vec{u}$	Rate of phase change	-	$\mathrm{m\,s^{-1}}$
$\vec{q}_i, \vec{q}_w$	Heat flux in ice/water	-	$\mathrm{W\,m^{-2}}$
L	Latent heat of ice	334	$\mathrm{kJ\,kg^{-1}}$

Table 1.2 List of symbols and values for boundary conditions and phase changes.

1.3 Weak form

The first step to solve the equations of thermal convection (Equation 1.1–1.4) using the finite element method (FEM), is to express them in the weak form. This is done by multiplying by a test function and integrating over the domain.

Continuity equation

First, for the continuity equation (Equation 1.1):

$$\int_V \chi \, (\nabla \cdot \vec{v}) \, \mathrm{d}V = 0 \,, \tag{1.18}$$

where χ is scalar test function.

Momentum equation

The momentum equation (Equation 1.2) is more complex. Here, I first combine it with the constitutive relation for Newtonian incompressible fluid (Equation 1.4) to the form:

$$-\nabla p + \nabla \cdot \eta(\nabla \vec{v} + (\nabla \vec{v})^T) + \rho \vec{g} = \vec{0} \,. \tag{1.19a}$$

In this case, the test function $\vec{w}$ is a vector function, and after the integration over the domain

$$\int_V \vec{w} \cdot \left[-\nabla p + \nabla \cdot \eta(\nabla \vec{v} + \nabla^T \vec{v}) + \rho \vec{g} \right] \mathrm{d}V = 0 \,, \tag{1.19b}$$

additional modifications need to be applied to eliminate the second-order derivatives. First, the pressure part is modified using the product rule for divergence and then Gauss' theorem on the second term:

$$\begin{aligned} \int_V -(\vec{w} \cdot \nabla p) \, \mathrm{d}V &= \int_V (\nabla \cdot \vec{w}) p - (\nabla \cdot (p \vec{w})) \, \mathrm{d}V \\ &= \int_V (\nabla \cdot \vec{w}) p \, \mathrm{d}V - \int_S p (\vec{w} \cdot \vec{n}) \, \mathrm{d}S \,, \end{aligned} \tag{1.19c}$$

and the viscosity part:

$$\int_V \vec{w} \cdot (\nabla \cdot (2\eta\dot{\boldsymbol{\varepsilon}}))\,\mathrm{d}V = \int_V w_k \left(\frac{\partial 2\eta\dot{\varepsilon}_{k1}}{\partial x_1} + \frac{\partial 2\eta\dot{\varepsilon}_{k2}}{\partial x_2} \right) \mathrm{d}V \tag{1.19d}$$
$$= -\int_V 2\eta \left(\frac{\partial w_k}{\partial x_1}\dot{\varepsilon}_{k1} + \frac{\partial w_k}{\partial x_2}\dot{\varepsilon}_{k2} \right) \mathrm{d}V + \int_S 2\eta w_k(\dot{\varepsilon}_{k1}n_1 + \dot{\varepsilon}_{k2}n_2)\,\mathrm{d}S$$
$$= -\int_V 2\eta(\nabla\vec{w} : \dot{\boldsymbol{\varepsilon}})\,\mathrm{d}V + \int_S 2\eta(\vec{w} \cdot \dot{\boldsymbol{\varepsilon}} \cdot \vec{n})\,\mathrm{d}S$$
$$= -\int_V 2\eta[\nabla\vec{w} : \mathrm{sym}(\nabla\vec{v})]\,\mathrm{d}V + \int_S 2\eta(\vec{w} \cdot \dot{\boldsymbol{\varepsilon}} \cdot \vec{n})\,\mathrm{d}S\,,$$

where $\mathrm{sym}(\nabla\vec{v})$ is the symmetric part of the tensor $\nabla\vec{v}$. The resulting weak form of the momentum equation (Equation 1.19a) is:

$$\int_V (\nabla \cdot \vec{w})p - 2\eta[\nabla\vec{w} : \mathrm{sym}(\nabla\vec{v})] - \rho g(\vec{e_z} \cdot \vec{w})\,\mathrm{d}V + \int_S \vec{w} \cdot (\boldsymbol{t} \cdot \vec{n})\,\mathrm{d}S = 0\,. \tag{1.19e}$$

In the case of a free surface on the bottom, there needs to be considered the effect of hydrostatic pressure as stated in Equation 1.14. This in weak formulation means adding:

$$+\int_{S_{bot}} g(\rho_w y - \rho_0 D)\vec{n} \cdot \vec{\chi}\,\mathrm{d}S_{bot}\,, \tag{1.19f}$$

where D is the thickness of the shell and $\rho_w = 1000\ \mathrm{kg\,m^{-3}}$ is water density.

Heat transfer equation

The heat transfer equation (Equation 1.6) is multiplied by a scalar test function τ and integrated over the domain:

$$\int_V \tau \left(\rho_0 c_p \frac{\partial T}{\partial t} - \nabla \cdot (k\nabla T) + \rho_0 c_p(\vec{v} \cdot \nabla T) - Q \right) \mathrm{d}V = 0\,. \tag{1.20a}$$

The heat conduction part is further modified:

$$\int_V \tau\nabla \cdot (k\nabla T)\,\mathrm{d}V = -\int_V k(\nabla\tau \cdot \nabla T)\,\mathrm{d}V + \int_S \tau(k\nabla T \cdot \vec{n})\,\mathrm{d}S \tag{1.20b}$$
$$= -\int_V k(\nabla\tau \cdot \nabla T)\,\mathrm{d}V - \int_S \tau q_n\,\mathrm{d}S\,,$$

where the Fourier's law was used

$$\vec{q} = -k\nabla T. \tag{1.20c}$$

Finally, after substituting for the boundary conditions, the weak form of the Equation 1.6 is:

$$\int_V \rho_0 c_p \frac{\partial T}{\partial t}\tau + k(\nabla\tau \cdot \nabla T) + \rho_0 c_p(\vec{v} \cdot \nabla T)\tau - Q\tau\,\mathrm{d}V = 0\,. \tag{1.20d}$$

For the usage in the code, I need to transform the partial derivative $\partial T/\partial t$ to its discrete form. For that, I use the Crank–Nicolson semi-implicit scheme

$$
\begin{aligned}
&\int_V \rho c_p \frac{T - T_k}{\Delta t}\tau \\
&+ \frac{1}{2}(k(\nabla\tau \cdot \nabla T) + \rho c_p(\vec{v} \cdot \nabla T)\tau) \\
&+ \frac{1}{2}(k(\nabla\tau \cdot \nabla T_k) + \rho c_p(\vec{v} \cdot \nabla T_k)\tau) \\
&- Q\tau \,\mathrm{d}V = 0\,,
\end{aligned}
\tag{1.20e}
$$

where T_k is the temperature in the previous time step and Δt is the length of the time step.

1.4 Model setup in FEniCS

Free surface equation

The Dirichlet boundary condition describing a free surface (Equation 1.12) contains a spatial derivative of the topography, therefore, it needs to be implemented differently from other boundary conditions. Following Juntunen and Stenberg [2009], I will use Nitsche's method for general boundary conditions. This allows me to rewrite the boundary condition as a Laplace equation in the form

$$
\Delta h = 0\,, \tag{1.21}
$$

with a general boundary condition

$$
\frac{\partial h}{\partial n} = \frac{1}{\epsilon}(h_0 - h) + g\,, \tag{1.22}
$$

where $\epsilon > 0$ is a parameter. When $\epsilon \to 0$, the solution of Equation 1.21 converges to the Dirichlet boundary condition and with $\epsilon \to \infty$ it converges to the Neumann boundary condition. Similar to the other equations, this equation needs to be converted to its weak form. With test function ϕ, I adopt the weak form from Kihoulou [2019]. For h_{top}, the top boundary weak form reads:

$$
\begin{aligned}
0 = &\int_V \frac{\partial h_{top}}{\partial y}\frac{\partial \phi}{\partial y}\,\mathrm{d}V - \int_{S_{top}} \frac{\partial h_{top}}{\partial y}\phi\,\mathrm{d}S_{top} \\
&- \int_{S_{top}} \left[\Delta h_{top} + \Delta t\left(\frac{\partial h_{top}}{\partial x}v_x - v_y\right)\right]\left(\frac{\partial \phi}{\partial y} - \frac{\phi}{\gamma h_E}\right)\mathrm{d}S_{top}\,,
\end{aligned}
\tag{1.23}
$$

where $\gamma > 0$ is a stabilization parameter, h_E is the length of an element in the x direction, and $\Delta h_{top} = h_{top}(t) - h_{top}(t - \Delta t)$.

For the bottom boundary, I need to take into account the phase change, which results in the following weak form:

$$
\begin{aligned}
0 = &\int_V \frac{\partial h_{bot}}{\partial y}\frac{\partial \phi}{\partial y}\,\mathrm{d}V - \int_{S_{bot}} \frac{\partial h_{bot}}{\partial y}\phi\,\mathrm{d}S_{bot} \\
&- \int_{S_{bot}} \left[\Delta h_{bot} + \Delta t\left(\frac{\partial h_{bot}}{\partial x}(v_x + u_x) - (v_y + u_y)\right)\right]\left(\frac{\partial \phi}{\partial y} - \frac{\phi}{\gamma h_E}\right)\mathrm{d}S_{bot}\,,
\end{aligned}
\tag{1.24}
$$

where $\Delta h_{bot} = h_{bot}(t) - h_{bot}(t - \Delta t)$ and $\vec{u}$ is the rate of the phase change according to Equation 1.16. The boundary conditions for the lateral boundaries and for the boundary opposite to the free boundary are the following:

$$\frac{\partial h_i}{\partial x} = 0 \quad \text{on } \mathrm{S_{side}}\,,$$
$$\frac{\partial h_i}{\partial y} = 0 \quad \text{on } \mathrm{S_{opposite}}\,,$$

where the lower index i represents either the top or bottom boundary, for which the S_{opposite} represents S_{bot} and S_{top} respectively.

Mesh movement

The deformation of the computational domain is solved using the ALE method [Scovazzi and Hughes, 2007]. Before moving the mesh, it is necessary to prescribe the displacement to the interior of the mesh. This is achieved by computing a Laplace equation with the Dirichlet boundary conditions corresponding to the deflection of the top and bottom boundary computed from free surface equations 1.23 and 1.24,

$$\begin{aligned} \Delta h_2 &= 0 \quad \text{in } V, \\ h_2 &= h_{top} \quad \text{on } \mathrm{S_{top}}, \\ h_2 &= h_{bot} \quad \text{on } \mathrm{S_{bot}}, \\ h_2 &= 0 \quad \text{on } \mathrm{S_{side}}, \end{aligned} \tag{1.25}$$

which, in the weak form, reads

$$\int_V \nabla h_2 \cdot \nabla \nu \,\mathrm{d}V = 0\,, \tag{1.26}$$

with ν being the test function.

Since the velocity in the advection term in Equation 1.3 is Eulerian (i.e., expressed with respect to a fixed mesh) it needs to be corrected for the velocity of the mesh movement,

$$\vec{v}_{mesh} = \frac{h_2(t) - h_2(t - \Delta t)}{\Delta t} \vec{e}_y\,. \tag{1.27}$$

Stabilization

When dealing with a free surface, additional stabilization needs to be added to the right side of momentum equation (Equation 1.2) to prevent the "drunken sailor effect" [Kaus et al., 2010]. The stabilization terms for the top and bottom boundaries in the weak form read

$$-\int_{S_{top}} \lambda g \rho_0 \left(1 - \alpha(T - T_0)\right) \Delta t \left(\vec{n} \cdot \vec{v}\right) \vec{e}_y \cdot \vec{w} \,\mathrm{d}S_{top}\,, \tag{1.28}$$

$$+\int_{S_{bot}} \lambda g \left(\rho_w - \rho_0 \left(1 - \alpha(T - T_0)\right)\right) \Delta t \left(\vec{n} \cdot \vec{v}\right) \vec{e}_y \cdot \vec{w} \,\mathrm{d}S_{bot}\,. \tag{1.29}$$

The second stabilization that needs to be implemented is related to the fact that both top and bottom boundaries are free. In that case, the solution of the velocity in the vertical direction is non-unique, as it is determined up to a constant. That is why the velocity after solving the Stokes problem (Equations 1.1, 1.2) needs to be corrected as follows to prevent motion of the shell as a whole:

$$\vec{v}_{corr} = \vec{v} - \frac{\vec{e}_y}{l} \int_S v_y \, \mathrm{d}S_{top} \,, \tag{1.30}$$

where l is the length of the boundary and $\vec{v}$ is the velocity computed from the Stokes problem.

Time step

I use an adaptive time step, based on the CFL (Courant-Friedrichs-Lewy) criterion

$$\Delta t_{\mathrm{cond}} = c_{\mathrm{CFL}} \frac{x_{\mathrm{min}}^2 \rho}{k(T)} \,, \tag{1.31}$$

$$\Delta t_{\mathrm{conv}} = c_{\mathrm{CFL}} \frac{x_{\mathrm{min}}}{v_{\mathrm{max}}} \,, \tag{1.32}$$

where Δt_{cond} is the conduction time step and Δt_{conv} is convection time step. The constant C_{CFL} is set as 0.5. In addition, I introduce a criterion that limits the movement of the mesh in a single time step to 100 m:

$$\Delta t_{\mathrm{mesh}} = c_{\mathrm{CFL}} \frac{100\,\mathrm{m}}{v_{\mathrm{mesh,\ max}}} \,. \tag{1.33}$$

The final time step is set to the minimum of them,

$$\Delta t = \min(\Delta t_{\mathrm{cond}},\, \Delta t_{\mathrm{conv}},\, \Delta t_{\mathrm{mesh}}) \,. \tag{1.34}$$

Program structure

This is an overview of the algorithm used.

Algorithm 1 Main simulation

```
Import required libraries
Set up parallelization (MPI)

Define mesh and boundaries
Define function spaces

Apply boundary conditions
Define material properties and physical parameters
Define all equations

Compute initial temperature distribution
Set up heat flux anomaly

while Simulation time < End time and not stabilized do
    Solve Stokes problem for velocity and pressure (1.1, 1.19a)
    Solve heat equation for temperature evolution (1.3)
    Solve top and bottom free surface equations (1.12, 1.15)
    Solve displacement of the mesh (1.25)

    Update free surface positions using ALE method
    Save results to output files
    Compute time step for next iteration
end while
```

1.5 Program testing

The program was tested using the benchmark by Blankenbach et al. [1989] and comparing the results with results obtained by various participants of this benchmark. The benchmark consists of three cases, all with immovable boundaries. The results were compared by computing the Nusselt number:

$$Nu = \frac{q_{tot}}{q_{cond}}\,, \tag{1.35}$$

where q_{tot} is total heat flux and q_{cond} is conductive heat flux over the top boundary, and root mean square velocity,

$$v_{rms} = \frac{h}{\kappa}\left(\frac{1}{hl}\int_0^l \int_0^h \vec{v}\cdot\vec{v}\,\mathrm{d}y\,\mathrm{d}x\right)^{\frac{1}{2}}\,, \tag{1.36}$$

where κ is the thermal diffusivity. The values used in the benchmark are displayed in Table 1.3.

Symbol	Meaning	Value	Unit
ΔT	Temperature contrast	1000	K
ρ_0	Density	4×10^3	kg/m^3
h	Height of the domain	10^6	m
κ	Thermal diffusivity	10^{-6}	m^2/s
g	Gravity acceleration	10	m/s^2
α	Thermal expansion coefficient	2.5×10^{-5}	1/K
ν	Kinematic viscosity	2.5×10^{19} (1a)	m^2/s
		2.5×10^{18} (1b)	m^2/s
		2.5×10^{17} (1c)	m^2/s
ν_0	Kinematic viscosity at surface	2.5×10^{19} (2)	m^2/s
c_p	Heat capacity	1.25×10^3	J K/kg
Q	Volumetric heating rate	5×10^{-9}	W/m^3

Table 1.3 List of symbols and values used in the benchmark.

Case 1

In this case, convection is studied with constant viscosity in a square box (aspect ratio 1) with free slip conditions prescribed on all boundaries. The temperature is fixed at the bottom and top boundary and the heat flux on the sides is set to zero. Case 1 has three subcases (1a-c) for different values of the Rayleigh number (1a - 10^4, 1b - 10^5, 1c - 10^6), corresponding to the different viscosities displayed in the Table 1.3.

For $Ra = 10^4$, the stabilized values of the Nusselt number and the root mean square velocity are shown in Table 1.4 and plotted over time in Figure 1.2.

Number	**Calculated Value**	**Reference Value**	**Error (%)**
Nu	4.88796	4.88441	0.0727
v_{rms}	42.8653	42.8649	0.00093

Table 1.4 Comparison of calculated and reference values for Nu and v_{rms} for case 1a.

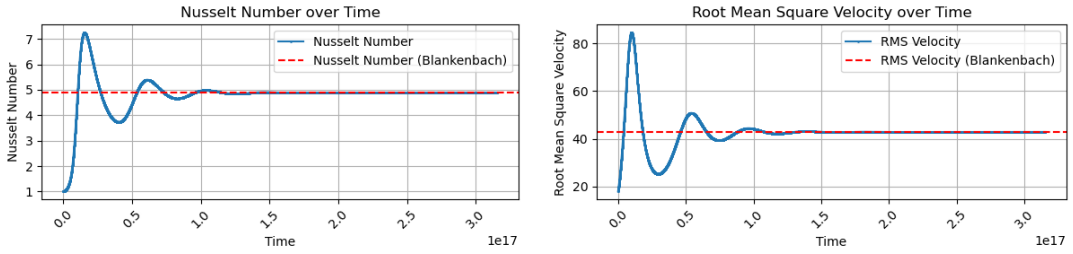


Figure 1.2 Nusselt number (left) and root mean square velocity (right) for case 1a.

In the case of $Ra = 10^5$, the values are displayed in Table 1.5 and plotted in Figure 1.3.

Number	Calculated Value	Reference Value	Error (%)
Nu	10.5708	10.5341	0.3484
v_{rms}	193.214	193.2145	0.00029

Table 1.5 As in Table 1.4 but for case 1b.

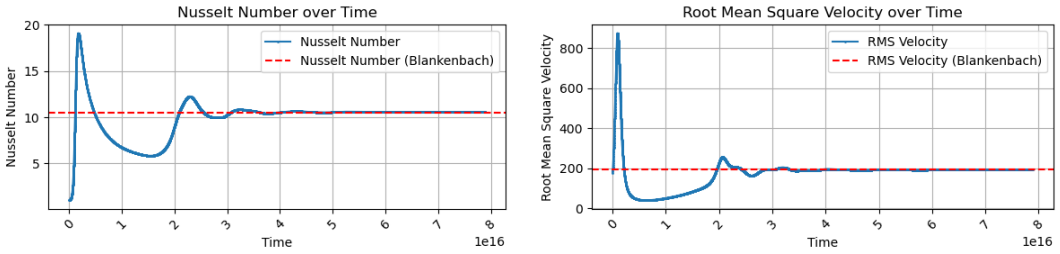


Figure 1.3 As in Figure 1.2 but for case 1b.

The last value of $Ra = 10^6$ leads in my model to stabilized values of Nusselt number and root mean square velocity displayed in table 1.6 and plotted in Figure 1.4.

Number	Calculated Value	Reference Value	Error (%)
Nu	22.3268	21.9725	1.587
v_{rms}	833.978	833.99	0.00144

Table 1.6 As in Table 1.4 but for case 1c.

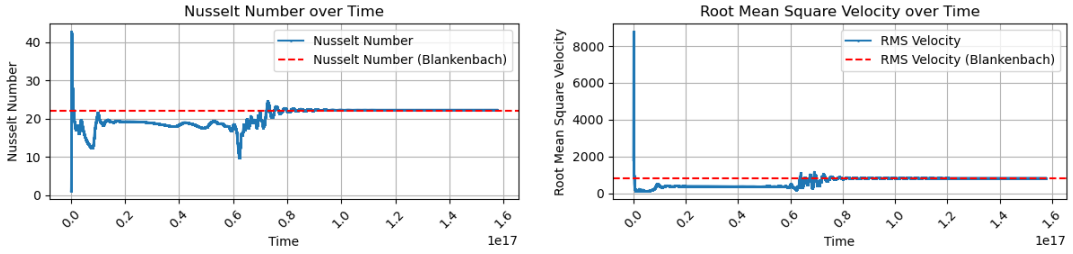


Figure 1.4 As in Figure 1.2 but for case 1c.

The error of the Nusselt number in case 1c, as shown in Table 1.6, is 1.587%. This error is induced by computing Equation 1.3 as a second-order differential equation and not as two first-order equations. My approach is easier to implement and faster to compute. Compared with other simplifications and uncertainties, such as those associated with the viscosity value and the influence of the grain size, the error introduced by this method is relatively minor and does not significantly affect the overall validity of the results.

Case 2

In case 2, the aspect ratio and boundary conditions remain the same as in case 1. The only difference is that now I use temperature-dependent viscosity prescribed as follows:

$$\nu(T) = \nu_0 \exp\left(\frac{-\ln(1000)T}{\Delta T}\right), \tag{1.37}$$

where ν_0 is the kinematic viscosity given in Table 1.3. The stabilized values of the Nusselt number and the root means square velocity are presented in Table 1.7 and plotted in Figure 1.5.

Number	Calculated Value	Reference Value	Error (%)
Nu	10.0833	10.0660	0.172
v_{rms}	480.200	480.433	0.049

Table 1.7 Comparison of calculated and benchmark values for case 2a.

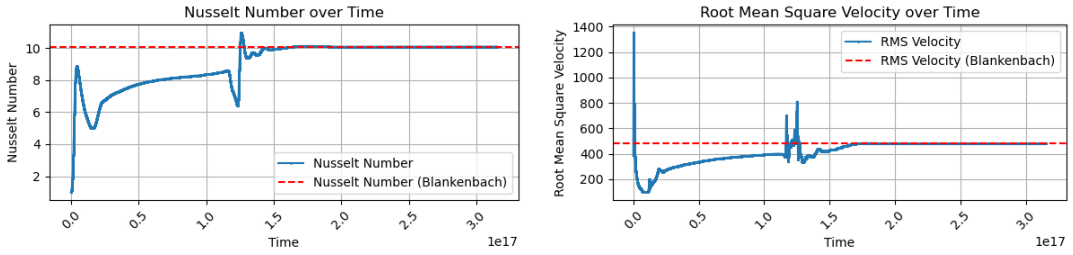


Figure 1.5 Nusselt number (left) and root mean square velocity (right) for case 2.

Case 3

In case 3, I am adding an internal heating to the heat transfer equation. Additionally, the boundary conditions change from free-slip to no-slip at the top and bottom boundary, and instead of prescribing temperature at the bottom boundary, a zero temperature gradient is imposed, i.e., $\partial T/\partial y = 0$. The aspect ratio is 1.5. This case leads to an oscillatory quasi-periodic state. I compare the extremes of these oscillations for the Nusselt number and root mean square velocity (displayed in Figure 1.6) in the Table 1.8.

Number	Calculated Value	Reference Value	Error (%)
Nu_{max1}	7.3799	7.379	0.012
Nu_{max2}	7.21837	7.196	0.311
Nu_{min1}	6.81302	6.796	0.250
Nu_{min2}	6.47847	6.468	0.162
v_{max1}	60.1705	60.367	0.326
v_{max2}	57.8936	57.430	0.807
v_{min1}	31.9808	31.981	0.001
v_{min2}	30.2896	30.320	0.100

Table 1.8 Comparison of extremes of Nusselt number and root mean square velocity for case 3.

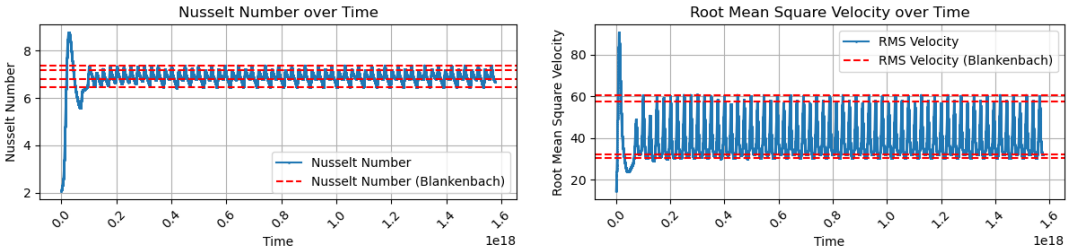


Figure 1.6 Nusselt number (left) and root mean square velocity (right) for case 3.

Free surface

Although not in the benchmark, free surface is an important part of the program, as I am investigating mechanisms behind the formation of depressions on the ice shell surface. Testing of free surface implementation was done by returning to case 1a with the Rayleigh number of 10^4 and implementing a free surface at the top boundary. For the testing itself, I compared the free surface calculated with the ALE method with the dynamic topography, which is calculated as follows:

$$h_{top} = -\frac{\vec{n} \cdot \boldsymbol{t} \cdot \vec{n}}{\rho g}. \tag{1.38}$$

In Figure 1.7, the topography of the top boundary at steady state is compared with the deflection of the top left corner point over time. The results indicate that both methods yield consistent outcomes, with the relative difference of the top left point in the steady state (illustrated in the right panel) amounting to approximately 1.51%.

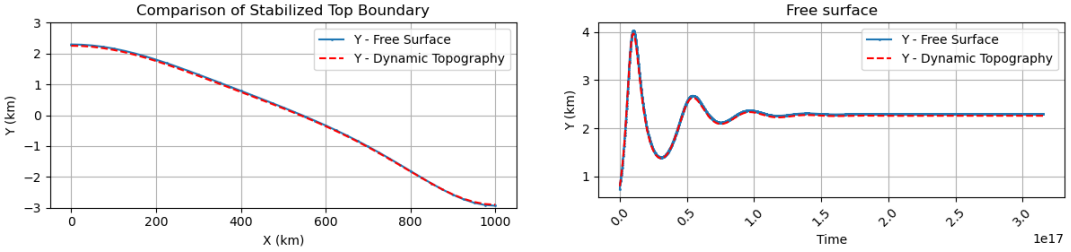


Figure 1.7 Stabilized surface (left) and deflection of specific point over time (right).

2 Results

2.1 Parametric study

The scenario tested in this thesis was the response of the ice shell to the heat flux anomaly from the ocean underneath. I considered several different amplitudes of the heat flux anomaly (ranging from 0.1 to 0.9 W m^{-2}) and three different thicknesses of the ice shell (20, 30 and 40 km).

The heat flux anomaly was represented by a Gaussian peak in the y component of the oceanic heat flux, with different amplitudes and widths (see Table 2.1). During the simulation, the average heat flux slightly increased due to the progressive thinning of the ice shell, which caused a small rise in the heat flux at the ice-water boundary. For this reason, all the heat fluxes presented below correspond to the stabilized stage of the simulation.

The cut-off viscosity, as explained in Section 1.1, is the upper restriction for the viscosity. I chose the value $\eta_{max} = 10^{21}$ Pa s, motivated by extremely long computation times (up to two weeks), however, the choice might slightly affect the amplitude of the topography [Kihoulou et al., 2023]. For one of the simulations, I tested a higher cut-off viscosity $\eta_{max} = 10^{22}$ Pa s. In all simulations, the reference viscosity η_0 in Equation 1.5 was set to 10^{16} Pa s.

N	D [km]	σ [km]	A [W m^{-2}]	η_{max} [Pa s]	max h_{bot} [km]	max $\lvert h_{top}\rvert$ [km]	$\tilde{\tau}$ [Myr]	Remark
1	20	3.33	0.245	10^{21}	12.5	0.402	11.6	
2	20	3.33	0.380	10^{21}	15.5	0.468	9.6	
3	20	3.33	0.571	10^{21}	17.3	0.541	9	see Section 2.2
4	30	5	0.157	10^{21}	16.4	0.579	14.8	
5	30	5	0.238	10^{21}	21.6	0.690	14.8	
6	30	5	0.348	10^{21}	25.05	0.820	15.4	see Section 2.6
7	20	6.67	0.644	10^{21}	17.1	1.44	9.6	see Section 2.4
8	40	6.67	0.863	10^{21}	37.4	1.52	> 6.6	see Section 2.5
9	20	3.33	0.755	10^{22}	18.3	0.214	> 3.8	see Section 2.6

Table 2.1 Model parameters tested in this study together with resulting values of maximum surface (max $\lvert h_{top}\rvert$) and ice-water interface (max h_{bot}) deflections. In the table, N is the model number, D is the thickness of the ice shell, σ and A are the half-width and the amplitude of the Gauss function, respectively, and $\tilde{\tau}$ is the characteristic time of the deformation.

2.2 Typical simulation

In this section, I will show the time evolution of a typical simulation. Figure 2.1 shows the prescribed heat flux and its shape for model 3 from Table 2.1

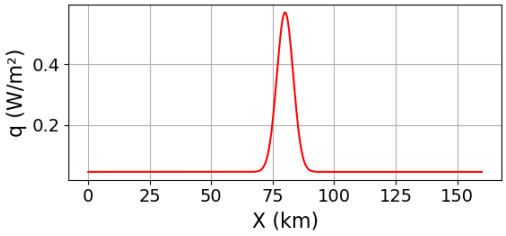


Figure 2.1 Prescribed heat flux in model 3.

while Figure 2.2 shows the time evolution of the temperature field.

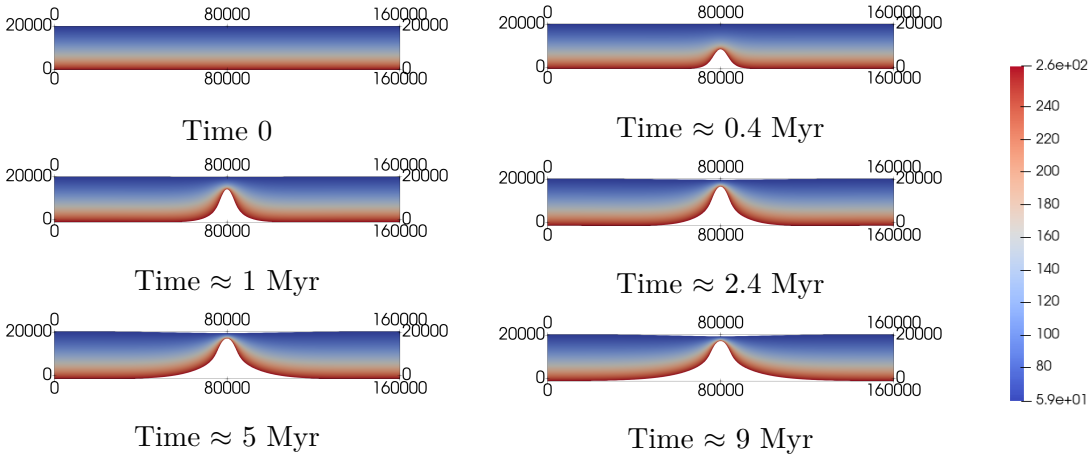


Figure 2.2 Evolution of the temperature and shape of the ice shell in model 3.

The bottom boundary almost fully stabilized after 2.4 Myr; however, the response of the upper boundary was much slower, as it took 9 Myr. The time scales are illustrated in Figure 2.3.

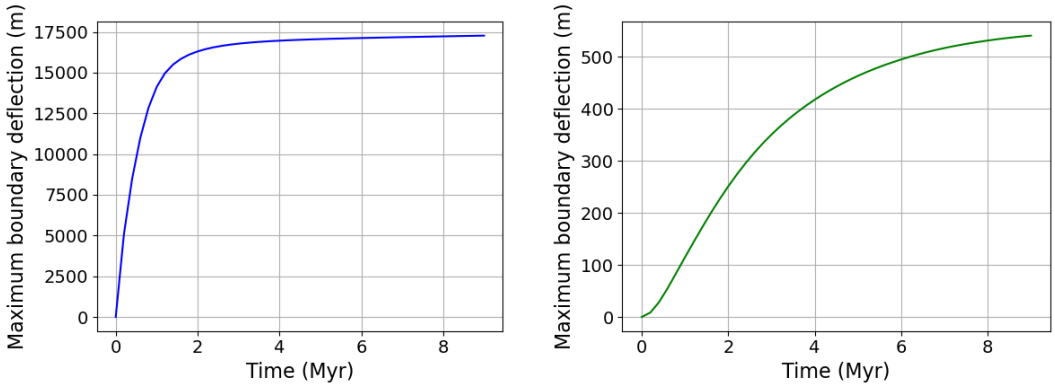


Figure 2.3 Amplitude of the bottom (left) and top (right) boundary deflections as a function of time in model 3.

2.3 Effect of the ice shell thickness

For an initial analysis and to better understand the ice shell response to a heat flux anomaly originating from the ocean, I tested different combinations of the amplitudes of the heat flux and ice shell thicknesses (see Figure 2.4). Because some of the simulations had computational times longer than two weeks, I was not able to systematically explore the space of combinations of parameters. Figure 2.4 shows the maximum value of the top boundary deflection and its dependence on the heat flux amplitude.

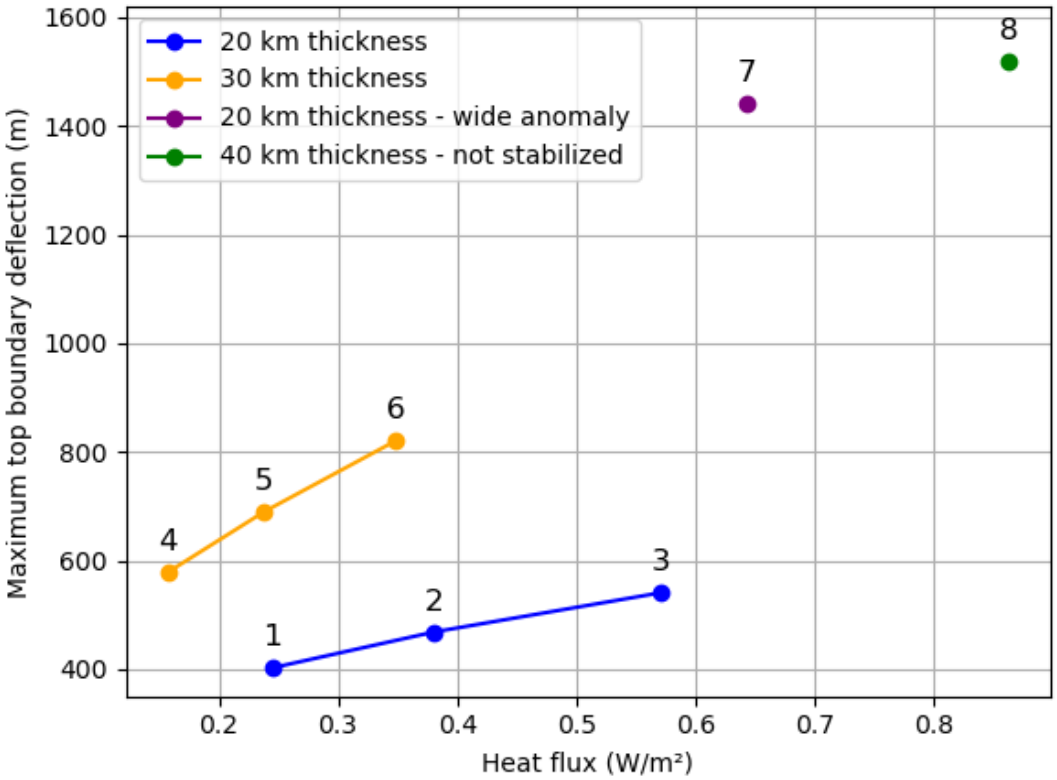


Figure 2.4 Maximum top boundary deflection as a function of the heat flux anomaly amplitude. The numbers of the points correspond to the numbers of models in Table 2.1.

Since the simulations were extremely computationally demanding, I did not succeed in exploring all relevant combinations of the model parameters. The number of the tested models is relatively low to reliably determine the trends behind the system evolution. Nevertheless, it appears that the topographic amplitude increases with the increasing amplitude of the heat flux anomaly, and the deformation of the ice shell is primarily controlled by a combination of the ice shell thickness and the heat flux width. The comparison of models 3 and 7 suggests that the width of the heat flux anomaly might play the dominant role.

2.4 Effect of heat flux anomaly width

An example of a model with a wide heat flux anomaly is model 7 in Table 2.1. In this case, the heat flux has an amplitude almost the same as in simulation 3

shown in Figure 2.2, but it is two times wider (see Figure 2.5).

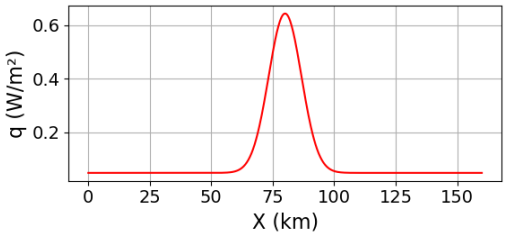


Figure 2.5 Heat flux anomaly considered in testing the effect of the heat flux anomaly width (model 7).

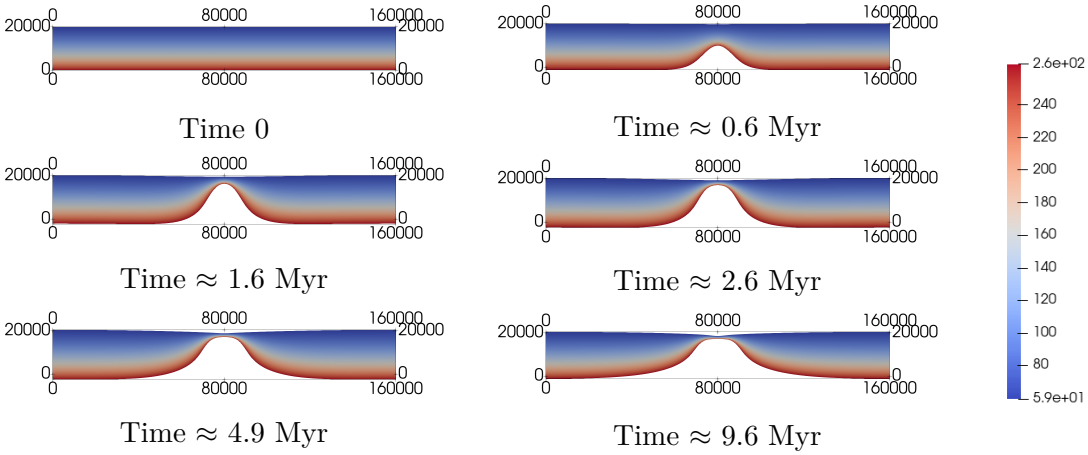


Figure 2.6 Evolution of the temperature and shape of the ice shell in model 7.

The evolution of temperature and deflection is shown in Figures 2.6 and 2.7.

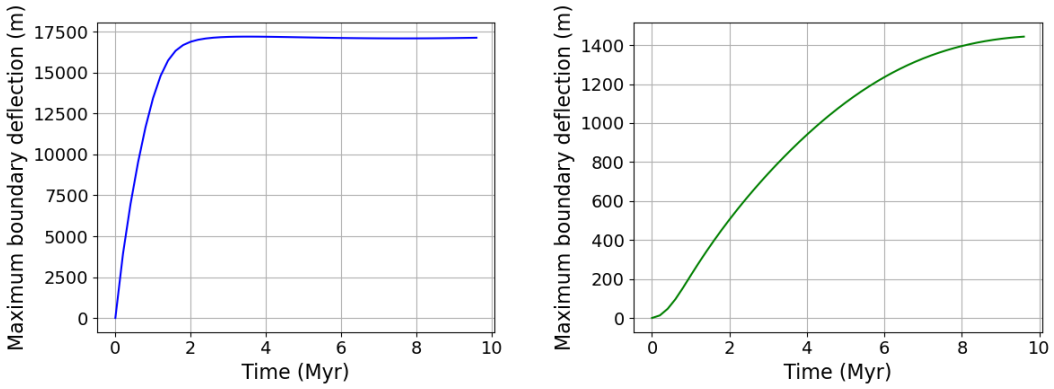


Figure 2.7 The evolution of the bottom (left) and top (right) boundary in model 7.

Comparison of Figures 2.2 and 2.6 shows that the width of the heat flux anomaly affects not only the amplitude of the deflection, but also the shape of the ice shell. The velocity field obtained for this simulation is illustrated in Figure 2.8. The highest velocities are located at the base of the upwelling zone near the center of the domain. This causes widening of the bottom topography anomaly, which

can also be observed in the evolution of the domain in Figure 2.6. It is also worth pointing out the fast downward velocities in the thinnest part of the ice shell, which is the reason behind the fast evolution of the top boundary.

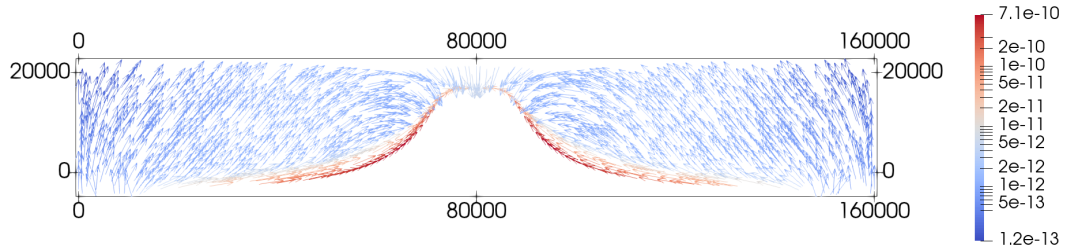


Figure 2.8 Velocity field for model 7 at $t = 5$ Myr. The velocity is given in m/s, and the color bar is logarithmic.

2.5 Results for the end-member thickness

I also carried out a simulation for a 40-km-thick ice shell. According to Čadek et al. [2016], this thickness corresponds to the maximum ice thickness on Enceladus. The prescribed heat flux has an amplitude and width given in Table 2.1 under the index 8. The simulation is not yet fully stabilized. Figure 2.9 shows the temperature field and the shape of the ice shell after approximately 6.6 million years. At this point, the amplitude of the surface topography reaches 1.52 km. It can be expected that, in the steady state, the surface deflection will be even deeper.

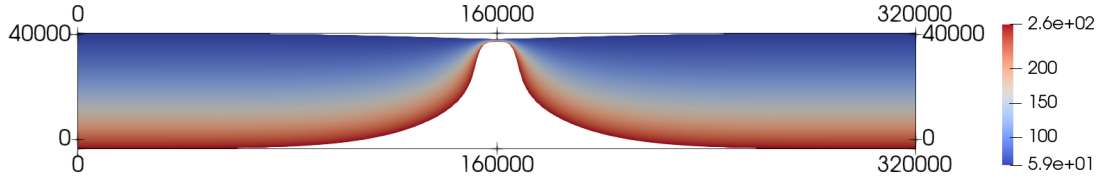


Figure 2.9 The temperature field after 6.6 million years.

2.6 Will the ice shell break?

The topographic depressions described by Schenk and McKinnon [2024] and Park et al. [2024] are characterized by the absence of fractures. This suggests that during the formation of the depressions, the stress never exceeded the failure threshold, which for ice is approximately 1 MPa. To assess whether the models developed in this study are compatible with observation, I computed the distribution of the second invariant of the deviatoric stress tensor,

$$\mathbf{t}_{\mathrm{II}}^{D} = 2\eta \sqrt{\frac{\frac{1}{2}\left(\nabla\vec{v} + (\nabla\vec{v})^{\top}\right) : \frac{1}{2}\left(\nabla\vec{v} + (\nabla\vec{v})^{\top}\right)}{2}} \tag{2.1}$$

and compared its magnitude with the tensile stress usually considered to be sufficient to rupture the ice shell.

First, I present the stress results of simulation 6 in Table 2.1.

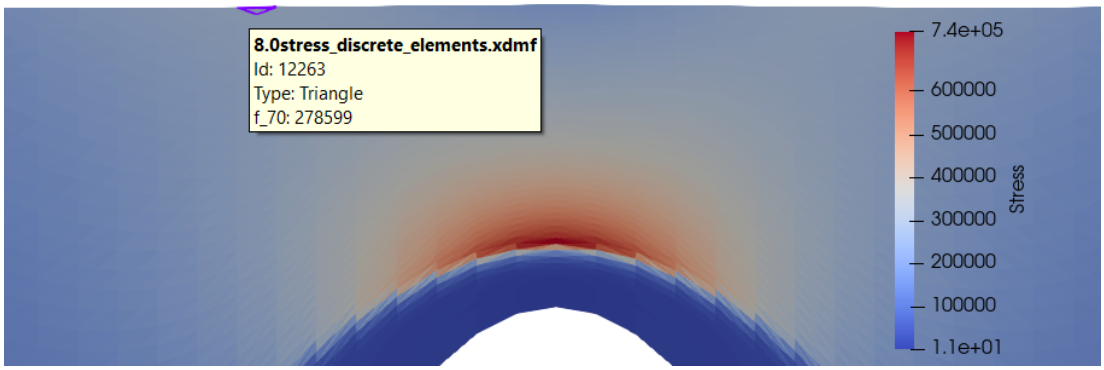


Figure 2.10 The second invariant of the deviatoric stress tensor for model 6.

The stress on the top boundary reaches only 0.28 MPa, which is not enough to break the ice shell (see Figure 2.10). However, in simulation 9 (see Table 2.1), I obtained stress values exceeding 1 MPa, thus sufficiently high to trigger the brittle deformation.

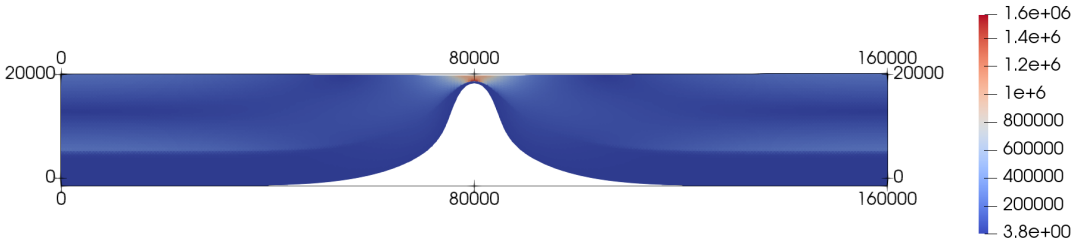


Figure 2.11 The second invariant of the deviatoric stress tensor and shape for model 9.

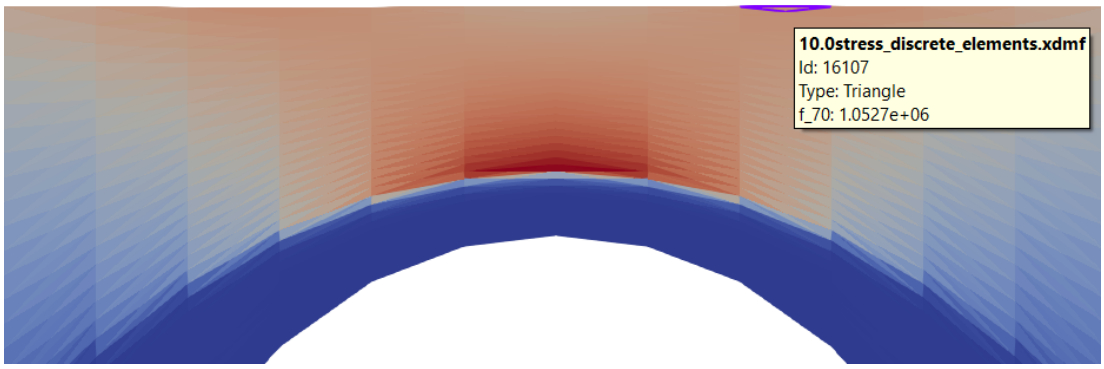


Figure 2.12 The second invariant of the deviatoric stress tensor - close up for model 9.

As shown in Figure 2.12, the computed stress reaches a value of 1.05 MPa. In the thinnest regions of the ice shell, stress levels exceed the estimated yield strength of ice, which suggests that high-amplitude heat flux anomalies could be responsible for the formation of fractured structures observed at the South Pole.

Discussion and Conclusions

The results indicate that variations in the heat flux from the ocean can generate deep depressions on Enceladus' surface, matching the values reported by Schenk and McKinnon [2024]. The computed amplitudes of the surface topography deflection in my simulations in the steady state range from 402 m for $D = 20$ km, $A = 0.243$ W m^{-2}, and $\sigma = 3.33$ up to 1444 m for $D = 20$ km, $A = 0.664$ W m^{-2}, and $\sigma = 6.67$. These surface depressions form over a timescale of approximately 10 million years. However, an important consideration is whether such heat flux anomalies can persist over this duration. The model presented by Choblet et al. [2017] suggests that the amplitudes of the heat flux anomalies originating from Enceladus' core can significantly exceed 1 W m^{-2}. This model also suggests that the highest amplitudes of the heat flux are presented at the South Pole (which is where Tiger Stripes are located) as well as along the meridians corresponding to longitudes of 90 and 270 degrees (which correspond to the locations of the depressions reported in Schenk and McKinnon [2024] and Park et al. [2024]). A recently published model by Bouffard et al. [2025] suggests that the heat generated in the core is transported through the ocean up to the ice-water boundary, despite the fact that thermal convection in the ocean is turbulent and characterized by strong zonal currents near the equator. It also shows that heat flux anomalies can be stable at timescales $>$ 10 Myr in regions little affected by the Coriolis forces, at which, according to Schenk and McKinnon [2024] and Park et al. [2024], the depressions investigated in this thesis are located.

Simulations were performed using relatively low values of surface ice viscosity ($\eta_{max} = 10^{21}$). That is relatively low, considering the conditions at Enceladus' surface (with temperatures below 60 K), this choice might slightly affect the amplitude of the topography [Kihoulou et al., 2023]. However, it is possible that the near-surface ice is not fully consolidated and its effective viscosity may be rather low. The effect of the cut-off viscosity on the solution will need to be verified through further simulations.

It appears that the topographic amplitude might be strongly influenced by the width of the heat flux anomaly, and may be comparable to the observed amplitudes even for smaller heat flux variations than those predicted by Choblet et al. [2017]. This hypothesis should be tested in future work by systematically exploring the model parameter space.

The results suggest that stress increases significantly in regions of the ice shell thinning and, in some cases, may exceed the tensile strength of ice. This fact would lead to brittle damage at the surface and possibly to the formation of surface structures similar to Tiger Stripes on the South Pole. Including these effects will require a more realistic description of ice rheology, incorporating elasto-plastic behavior and stress-dependent viscosity. It will also be necessary to modify the geometry of the computational domain to account for the curvature of Enceladus.

Overall, the model confirms that the ice shell's response to the variations in heat flux from the ocean is likely to be the reason behind the 100-km-scale depressions observed at Enceladus' surface. The results also suggest that the same mechanism can be responsible for creating the Tiger Stripes on the South Pole. In future research, I would like to build on this work by focusing on the same scenario and implementing a more realistic description of the ice rheology.

Bibliography

B. Blankenbach, F. Busse, U. Christensen, L. Cserepes, D. Gunkel, U. Hansen, H. Harder, G. Jarvis, M. Koch, G. Marquart, et al. A benchmark comparison for mantle convection codes. *Geophysical Journal International*, 98(1):23–38, 1989.

M. Bouffard, G. Choblet, H. Amit, G. Tobie, O. Čadek, and F. Terra-Nova. Seafloor hydrothermal control over ocean dynamics in Enceladus. *Nature Astronomy*, page in press, 2025.

O. Čadek, G. Tobie, T. Van Hoolst, M. Massé, G. Choblet, A. Lefèvre, G. Mitri, R.-M. Baland, M. Běhounková, O. Bourgeois, et al. Enceladus's internal ocean and ice shell constrained from Cassini gravity, shape, and libration data. *Geophysical Research Letters*, 43(11):5653–5660, 2016.

E. Carnahan, N. S. Wolfenbarger, J. S. Jordan, and M. A. Hesse. New insights into temperature-dependent ice properties and their effect on ice shell convection for icy ocean worlds. *Earth and Planetary Science Letters*, 563:116886, 2021.

G. Choblet, G. Tobie, C. Sotin, M. Běhounková, O. Čadek, F. Postberg, and O. Souček. Powering prolonged hydrothermal activity inside Enceladus. *Nature Astronomy*, 1(12):841–847, 2017.

D. L. Goldsby and D. L. Kohlstedt. Superplastic deformation of ice: Experimental observations. *Journal of Geophysical Research: Solid Earth*, 106(B6): 11017–11030, 2001.

M. Juntunen and R. Stenberg. Nitsche's method for general boundary conditions. *Mathematics of computation*, 78(267):1353–1374, 2009.

B. J. P. Kaus, H. Mühlhaus, and D. A May. A stabilization algorithm for geodynamic numerical simulations with a free surface. *Physics of the Earth and Planetary Interiors*, 181(1-2):12–20, 2010.

M. Kihoulou. Viskoelastická deformace ledových těles ve sluneční soustavě. Bachelor thesis, Charles University, Faculty of Mathematics and Physics, 2019. URL `https://geo.mff.cuni.cz/theses/2019-Kihoulou-Bc.pdf`. Accessed: 2025-04-03.

M. Kihoulou, O. Čadek, J. Kvorka, K. Kalousová, G. Choblet, and G. Tobie. Topographic response to ocean heat flux anomaly on the icy moons of Jupiter and Saturn. *Icarus*, 391:115337, 2023.

T. B. McCord and C. Sotin. Ceres: Evolution and current state. *Journal of Geophysical Research: Planets*, 110(E5), 2005.

NASA/JPL-Caltech/Space Science Institute. A Tale of Two Hemispheres, 2015. URL `https://photojournal.jpl.nasa.gov/catalog/PIA18340`. Photographed: July 17. 2015.

R. S. Park, N. Mastrodemos, R. A. Jacobson, A. Berne, A. T. Vaughan, D. J. Hemingway, E. J. Leonard, J. C. Castillo-Rogez, C. S. Cockell, J. T. Keane, et al. The global shape, gravity field, and libration of Enceladus. *Journal of Geophysical Research: Planets*, 129(1):e2023JE008054, 2024.

F. Postberg, S. Kempf, J. Schmidt, N. Brilliantov, A. Beinsen, B. Abel, U. Buck, and R. Srama. Sodium salts in E-ring ice grains from an ocean below the surface of Enceladus. *Nature*, 459(7250):1098–1101, 2009.

P. M. Schenk and W. B. McKinnon. New global topography of Enceladus: Hypsometry, basins, spherical harmonics, shell thickness, and true polar wander revisited. *Icarus*, 408:115827, 2024.

G. Scovazzi and T. J. R. Hughes. Lecture Notes on Continuum Mechanics on Arbitrary Moving Domains. Sandia National Laboratories, 2007.

O. Souček, M. Běhounková, O. Čadek, J. Hron, G. Tobie, and G. Choblet. Tidal dissipation in Enceladus' uneven, fractured ice shell. *Icarus*, 328:218–231, 2019.

P. C. Thomas, R. Tajeddine, M. S. Tiscareno, J. A. Burns, J. Joseph, T. J. Loredo, P. Helfenstein, and C. Porco. Enceladus's measured physical libration requires a global subsurface ocean. *Icarus*, 264:37–47, 2016.

List of Figures

1 A Tale of Two Hemispheres. 6
2 Topography of Enceladus. 7

1.1 Sketch of the computational domain with boundary conditions. . 9
1.2 Nusselt number (left) and root mean square velocity (right) for case 1a. 17
1.3 As in Figure 1.2 but for case 1b. 18
1.4 As in Figure 1.2 but for case 1c. 18
1.5 Nusselt number (left) and root mean square velocity (right) for case 2. 19
1.6 Nusselt number (left) and root mean square velocity (right) for case 3. 20
1.7 Stabilized surface (left) and deflection of specific point over time (right). 20

2.1 Prescribed heat flux in model 3. 23
2.2 Evolution of the temperature and shape of the ice shell in model 3. 23
2.3 Amplitude of the bottom (left) and top (right) boundary deflections as a function of time in model 3. 23
2.4 Maximum top boundary deflection as a function of the heat flux anomaly amplitude. 24
2.5 Heat flux anomaly considered in testing the effect of the heat flux anomaly width (model 7). 25
2.6 Evolution of the temperature and shape of the ice shell in model 7. 25
2.7 The evolution of the bottom (left) and top (right) boundary in model 7. 25
2.8 Velocity field for model 7 at $t = 5$ Myr. 26
2.9 The temperature field after 6.6 million years. 26
2.10 The second invariant of the deviatoric stress tensor for model 6. . 27
2.11 The second invariant of the deviatoric stress tensor and shape for model 9. 27
2.12 The second invariant of the deviatoric stress tensor - close up for model 9. 27

List of Tables

1.1 List of symbols and values for Chapter 1.1. 9
1.2 List of symbols and values for Chapter 1.2 11
1.3 List of symbols and values used in the benchmark. 17
1.4 Comparison of Nu and v_{rms} for case 1a. 17
1.5 As in Table 1.4 but for case 1b. 18
1.6 As in Table 1.4 but for case 1c. 18
1.7 Comparison of Nu and v_{rms} for case 2a. 19
1.8 Comparison of Nu and v_{rms} for case 3. 19

2.1 Model parameters tested in this study together with resulting values. 22